ADVANCED MATERIALS TECHNOLOGIES
www.advmattechnol.de

Plasma Focused Ion Beam Tomography for Accurate Characterization of Black Silicon Validated by Full Wave Optical Simulation

Yu Zhang, Tom Veeken, Shaozhou Wang, Giuseppe Scardera, Malcolm Abbott, David Payne, Albert Polman,* and Bram Hoex**

Black silicon (BSi) is a branch of silicon material whose surface is specially processed to a micro/nanoscale structure, which can achieve ultra-low reflectance or ultra-high electrochemical reactivity. The diversity and complex surface structures of BSi make it challenging to commercialize BSi devices. Modeling and simulation are commonly used in the semiconductor industry to help in better understanding the material properties, predict the device performance, and provide guidelines for fabrication parameters' optimization. The biggest challenge for BSi device modeling and simulation is obtaining accurate input surface morphological data. In this work, the 3D models of challenging BSi textures are compared as obtained by atomic force microscopy (AFM) and plasma focused ion beam (PFIB) tomography techniques. In previous work, the PFIB tomography workflow toward the application of surface topography is optimized. In this work, the 3D models obtained from both AFM and PFIB are comprehensively compared, by using the surface models as inputs for finite-difference time-domain-based optical simulation. The results provide strong evidence that PFIB tomography is a better choice for characterizing highly roughened surface such as BSi and provides surface 3D models with better reliability and consistency.

1. Introduction

Silicon is one of the most widely used materials in the semiconductor industry due to its abundance and stable chemical and mechanical structure. It has been widely used in various applications, such as chips and microchips in electronic devices, photodiodes, photodetectors, and photovoltaic (PV) devices. A particular branch of silicon material is black silicon (BSi), the surface of which is specially processed to create a micro-/nanoscale texture.[1,2] As such, the optical performance of BSi is superior to the unprocessed silicon wafer with a planar surface, with extremely high optical absorption and low reflectance over a broad spectral range. However, due to the complex nature of the BSi surface structure, adapting the academic level BSi into a commercial device is challenging. For example, BSi with an extremely high aspect ratio will present challenges for making acceptable screen-printed contacts as used in silicon solar cells.[3] Furthermore, the increased surface area can result in inferior surface passivation.[4–6] Therefore, the state-of-the-art commercialized BSi devices are typically compromised to a less aggressive surface structure with nonoptimal optical properties.[7,8]

Semiconductor device fabrication involves multistep physical and chemical manufacturing process sequences.[9] Each of the variables involved in multistep processing could potentially bring uncertainties during manufacturing. As such, modeling and simulation are well-accepted concepts in the semiconductor industry. They provide guidelines for the optimal parameters for actual device fabrication and help researchers to rapidly understand

---

Y. Zhang, S. Wang, G. Scardera, M. Abbott, D. Payne, B. Hoex
School of Photovoltaic and Renewable Energy Engineering
University of New South Wales
Sydney, NSW 2052, Australia
E-mail: david.payne@mq.edu.au; b.hoex@unsw.edu.au

The ORCID identification number(s) for the author(s) of this article can be found under https://doi.org/10.1002/admt.202200068.

DOI: 10.1002/admt.202200068

T. Veeken, A. Polman
Center for Nanophotonics
NWO-Institute AMOLF
Science Park 104, Amsterdam 1098 XG, the Netherlands
E-mail: a.polman@amolf.nl

D. Payne
School of Engineering
Macquarie University
Sydney, NSW 2109, Australia

the new technology and its capability and economic potential. There are various commercially available simulation tools developed for the semiconductor industry. Simulation software packages, such as Sentaurus,[10] are designed to solve device performance comprehensively, but they are computationally expensive. Other software that provides fast approximate simulation, such as SunSolve,[11] usually focuses on one aspect of the device physics (such as the optical response) to enable efficient simulation and optimization toward a specific goal (such as maximizing optical absorption).

As BSi is a relatively new concept for the semiconductor industry, there are still many challenges for correctly simulating BSi device performance. It is, e.g., unknown how the nanotextured surface interacts with the pre- and post-manufacturing processes. For the PV industry, it is of great interest to understand exactly how the enlarged surface area impacts the dopant diffusion for emitter formation, how the passivation layer interacts with the complex surface texturing, and how the near-surface damage produced during BSi fabrication would affect the final energy conversion efficiency of the solar cell. To establish a precise and accurate BSi device performance simulation and a rapid modeling technique, it is vital that modeling of the material characteristics is first validated with the fundamental material properties.

The material characteristics of BSi that people care about most, such as optical performance and surface electrochemical reactivity, are linked to its surface morphology, i.e., the shape and dimension of the nanostructure.[1,2,12] However, it is challenging to probe the BSi surface properly in order to accurately quantify the texture's topography.[13,14] The most adopted surface topography characterization technique is atomic force microscopy (AFM), which measures the surface height data pixel by pixel with a scanning probe.[15–17] However, for BSi surfaces, the varied fabrication methods and processing parameters can result in a broad variety of nanostructure shapes, such as needle-like structures, grooves, hollow-like structures, cone-like structures, etc. Limited by its working principle, AFM is not able to detect structures that exceed the aspect-ratio dimensions of the probe or micro-nano hybrid structures that exceed the oscillation limits of the cantilever. AFM may be applicable for only a few types of BSi in cases where the surface structure is not too extreme. Moreover, it is incredibly challenging to avoid AFM imaging artifacts when characterizing very rough surfaces. These artifacts can be induced by a nonideal tip shape, tip bending, flexing, jumping effects, the adhesion forces forming between tip and sample, or nonoptimal scan settings.[18–20] The constant tip-sample interaction during the measurement of a highly roughened surface can also degrade or contaminate the AFM probe tip. Without using additional alternate techniques such as scanning electron microscopy (SEM), it can be challenging to determine the correctness of the 3D model rendered from an AFM scan, where the PFIB shows advantages as a viable alternative solution.

In our previous work, PFIB tomography was demonstrated as a potentially superior alternative for AFM, especially for probing complex structures such as a BSi surface.[14] Not only can PFIB tomography detect nonupright features that the AFM probe could not reach, but it also offers a less-biased 3D rendering model and enhanced consistency to avoid the AFM artefacts arising from the repetitive probe-sample interaction during the scanning process. However, in our previous work, the quality of the PFIB rendered 3D model was simply evaluated by visualizing and providing a simple comparison of surface statistics. The statistics, however, were not validated in any way with its correctness. To better evaluate the advantages of the PFIB 3D model over the AFM 3D model, this work focuses more on quantitative evaluation, and the validation will be checked against simulation results. In this work, we compare the quality of 3D rendered models of BSi surface textures obtained from AFM and plasma focused ion beam (PFIB) tomography. We evaluate the 3D models both qualitatively and quantitatively, by comparing the morphology with their SEM images, comparing the surface statistics, and evaluating the accuracy of the optical response generated by the surface models as determine by FDTD simulation.

The quality of the 3D model is evaluated by simulating the front surface reflectance. As there is no standard way to assess the accuracy of topographical measurements, the mismatch between the simulated measured reflectance was used as a metric to describe the accuracy of the reconstructed 3D model. The irregular shapes and sizes of BSi features, typically on the order of the wavelength of light, make it challenging to predict the light–surface interaction, making fast approximation methods (such as effective medium[21,22] and geometric optics[23,24]) typically not suitable for describing the optics of BSi textures. One of the most common tools to accurately calculate reflectance is the FDTD algorithm. Although it requires significantly more computational resources than the fast approximation methods, the FDTD simulation captures all light–matter interactions by solving Maxwell's equations. As such, simulated optical properties of BSi textures include resonant nanophotonic light–matter interactions that occur on length scales of the order of the wavelength.[21] Therefore, the FDTD simulation can be directly compared with experimental results.[25] Several previous studies have successfully applied FDTD to understand and model the optical behavior of nanotextured silicon.[26–28] Here, we use the convergence between the measured reflection [Reflection(%)] and the FDTD simulated Reflection(%) to evaluate the accuracy of the acquired 3D model quantitatively. We will use two different BSi samples in this work and show a good agreement in measured and simulated Reflection(%) when using the 3D model determined by PFIB. In contrast, the simulated reflectance based on the AFM 3D models showed a significant deviation from the measured results, particularly for the more extreme BSi sample. Our work provides strong evidence that the PFIB rendered 3D model can be used as a reliable simulation input for the FDTD algorithm to accurately model and predict the BSi wafer's front surface optical characteristics. In addition to the FDTD analysis, a thorough surface statistical comparison is also demonstrated. Some critical surface statistics will be reported for both the AFM 3D model and the PFIB 3D model which will aid the development of a fast approximation method for BSi optical simulation.[21,29] In addition, morphological parameters critical in the BSi electrical performance will also be compared across the AFM 3D model and the PFIB 3D model such as enhanced area factor and specific surface area.[30]

The results of this work may also be applicable to modeling other material fundamental properties, such as surface area-related electrochemical reactivity, the pre- and/or post thin-film interaction during device manufacturing, etc. It can be further developed to predict the completed BSi device performance, such as fast optical simulation[11,29,31] or current–voltage simulation[32] of completed BSi device with the addition of surface deposition layers and encapsulation layers.

2. Experimental Methodology

Two different BSi samples were used for this work, each with significantly different surface structures, in order to evaluate the quality of the rendered 3D surface models. Both BSi samples were fabricated by reactive ion etching (RIE) but under different fabrication conditions, which manifested different surface texturing finish. The sample designated as RIE1-BSi had relatively shallower and smaller groove-like features, while RIE2-BSi had relatively deeper inverted-hollow-like features. The 3D surface models for both samples were obtained from both PFIB tomography and AFM and were used as an input to the FDTD simulations. Three 3D surface models for both BSi samples were obtained: one from PFIB tomography, designated as RIE-PFIB; and two sets from AFM, designated as RIE-AFM-HQ (high quality) and RIE-AFM-LQ (low quality). Several critical surface-related statistics were then extracted to be used for the quantitative evaluation of the 3D model quality, including but not limited to the height distribution and the convergence of the FDTD simulated reflection to the measured reflection.

2.1. Sample Information

Two plasma textured silicon surfaces were fabricated using different RIE tools to achieve distinct surface morphologies.

The RIE1-BSi texture was fabricated on a polished 4 in. round silicon wafer etched using an STS DRIE Pegasus tool for 16 min. The reactive gases used for this sample were O_2 (100 sccm) and SF_6 (70 sccm). The coil power was 3 kW.

The RIE2-BSi texture was fabricated on a polished 6 in. round silicon wafer using an SPTS RIE system. The maskless RIE was conducted at room temperature in an O_2 and SF_6 plasma for 16 min, with a gas flow ratio of O_2:SF_6 = 1:1, chamber pressure of 24 mTorr, and a 13.56 MHz radio-frequency platen power of 100 W.

A representative plan view and cross-sectional view SEM images of both RIE1 and RIE2 are shown in **Figure 1**. It could be seen that the RIE1-BSi texture was relatively shallower and showed smaller groove-like features. The depth of the texturing was around 400 nm, with a smooth transition from the peak to the bottom. The RIE2-BSi texture had comparatively deeper inverted-hollow-like features with a depth of around 2 µm and nearly vertical sidewalls connecting the upper and lower plateaus. The high aspect-ration nature of the RIE2-BSi texture was likely to pose a challenge for AFM scanning characterization.

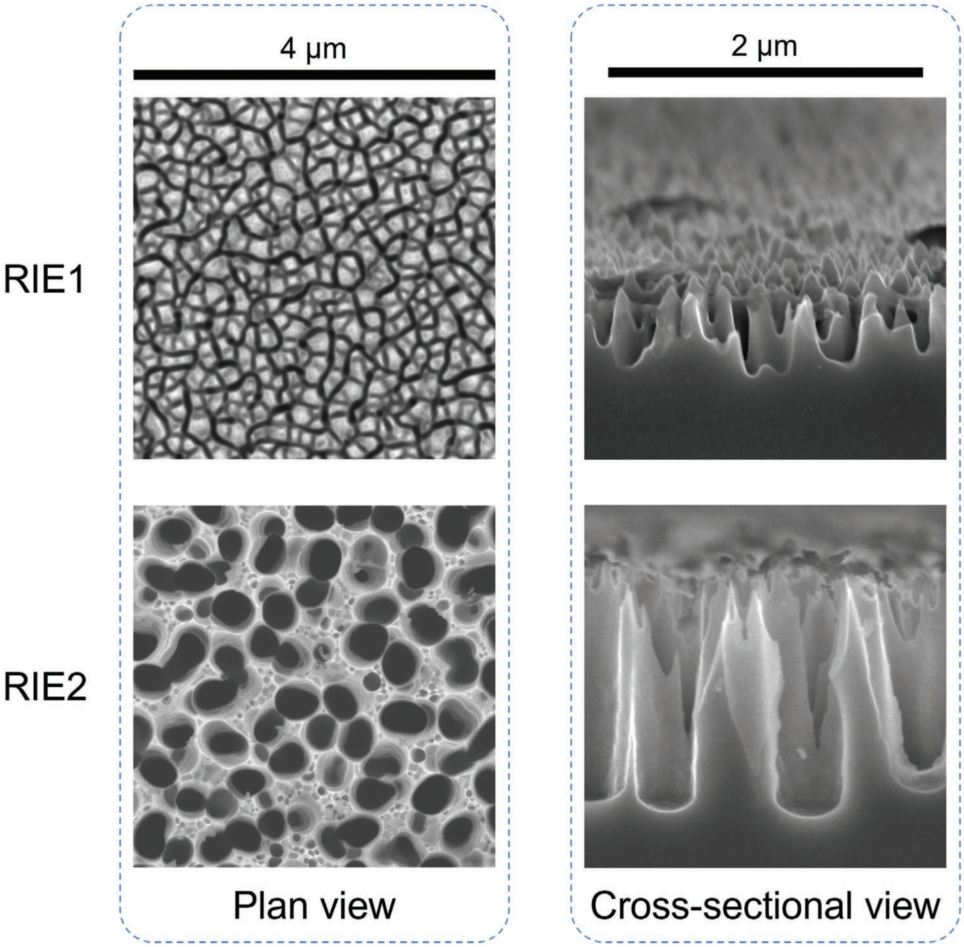

Figure 1. Plan view (left column) and cross-sectional view (right column) of RIE1 and RIE2 obtained using SEM.

2.2. Topographical Characterization

a) AFM

Topographical characterization of both BSi-RIE1 and BSi-RIE2 was conducted by JEOL JSPM 5400 MkII Environmental AFM. Two sets of AFM scans were obtained for each sample, named AFM-HQ and AFM-LQ; these represented repeat measurements carried out with different AFM probes. HQ and LQ stand for "high quality" and "low quality," respectively. AFM-LQ was considered a failed AFM attempt with visible artefacts observed in the final 3D surface model. The probes used for RIE1-AFM-LQ were DDESP Bruker AFM probes, while TESPD Bruker AFM probes were used for RIE2-AFM-LQ. AFM-HQ was considered an acceptable AFM attempt with probe choice and settings optimized and tuned to minimize artefacts in the final 3D surface model. The probes used for both RIE1-AFM-HQ and RIE2-AFM-HQ were TESPD Bruker AFM probes. All the AFM scans were done in tapping mode over an area of 10 µm by 10 µm, with a scan-interval of 19.53 nm and a scan rate of 0.215 Hz. To obtain optimal scan results, the tip velocity was tuned slightly around 4.30 µm s^{-1} to obtain optimal scan results.

b) PFIB tomography

Topographical characterization of both BSi-RIE1 and BSi-RIE2 was also conducted by PFIB tomography.

The PFIB tomography process contained three major parts:

1) *Sample preparation*: Both BSi samples were first embedded in a Durcupan resin before mounting into the microscopic stage. This was done to ensure that the SEM images did not contain artefacts, e.g., resulting from residual voids.
2) *Slice-and-view process*: The topographical BSi cross-sectional datasets were obtained using a ThermoFisher Helios G4 PFIB UXe PFIB-SEM DualBeam System. The automated slice-and-view process was controlled by Auto Slice and View 4 software, which consisted of repetitive PFIB milling of the sample (slice) and subsequent SEM imaging (view). In this experiment, a total of 1566 SEMs were collected. Each high-resolution SEM has an image resolution [width by height] of 6144 × 4376 pixels, with each pixel's dimension of 4.21×4.21 nm^2. With careful control of the PFIB beam profile, the slice thickness was optimized down to 10 nm.
3) *3D data reconstruction*: The SEM stack containing the specimen's cross-sectional information was processed by a sequence of imaging processing techniques, including image filtering and the translation to XYZ format compatible with established 3D surface data analysis software. The 3D surface data translated from the SEM stack had lateral dimensions of 21.62×15.21 µm^2.

A more comprehensive description of the PFIB method is presented in previously published work.[33,34]

3D surface models of BSi-RIE1 obtained from PFIB tomography, AFM-HQ, and AFM-LQ are shown in **Figure 2**. 3D surface model of BSi-RIE2 sample obtained from PFIB tomography, AFM-HQ, and AFM-LQ are shown in **Figure 3**.

c) Data Comparison

Based on the working principle of PFIB-SEM tomography, the height distribution was extracted from each cross-sectional SEM image obtained during the slice-and-view process, which revealed the true cross-sectional morphology, ensuring minimized bias and high data accuracy.

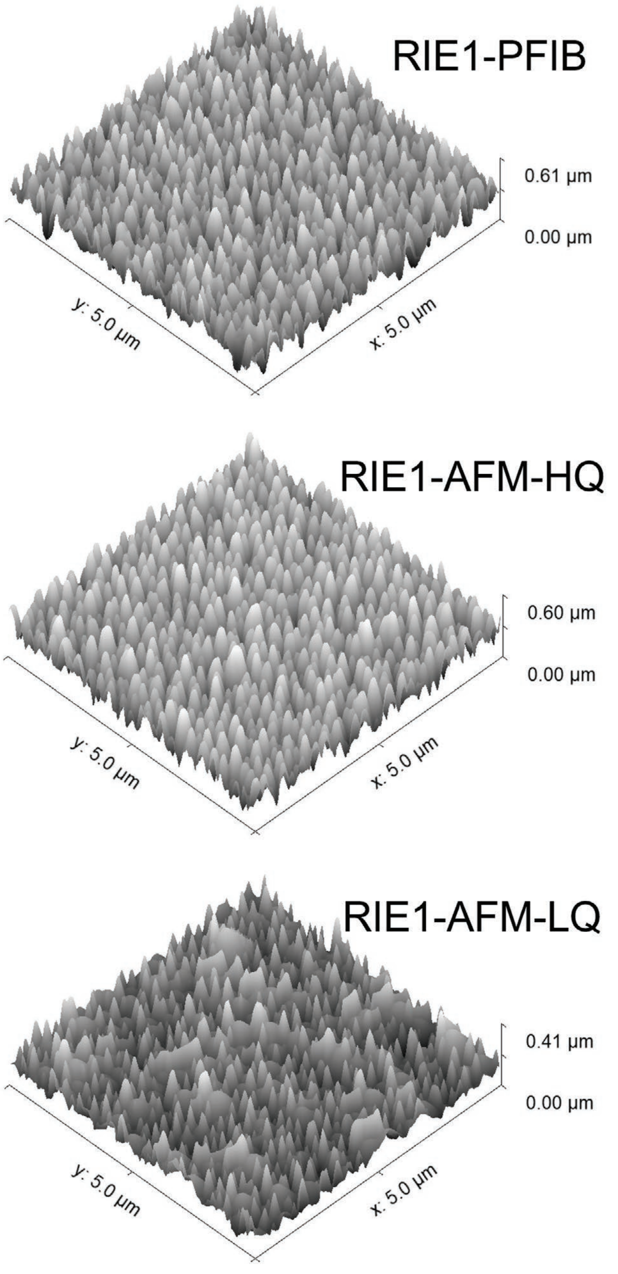

Figure 2. 3D surface model of RIE1 sample obtained from: a) PFIB tomography, b) AFM-HQ, and c) AFM-LQ.

After carefully choosing the AFM scanning probe and optimizing the probing parameters, the AFM-HQ scans for both RIE1-BSi and RIE2-BSi were obtained. The AFM-HQ achieved similar results to their PFIB 3D model in some apparent surface statistics, regardless of whether their appearance was similar to the SEM image. In comparison, AFM-LQ scans reported surface statistics deviate significantly from RIE-AFM-HQ and the PFIB 3D model. In particular, the RIE1-AFM-LQ model appeared to have multiple visible scan artifacts. The overall height was 0.2 µm shallower than the other two 3D models. For

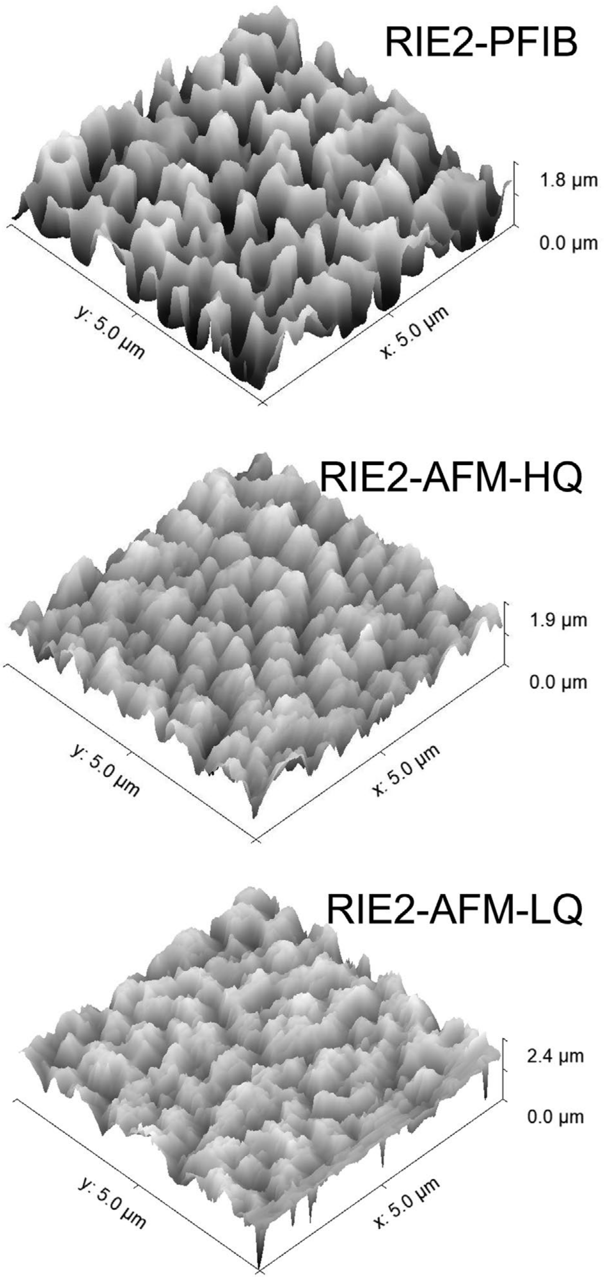

Figure 3. 3D surface model of RIE2 sample obtained from: a) PFIB tomography, and b) AFM-LQ, and c) AFM-LQ.

the RIE2-AFM-LQ model, due to the nature of the AFM working principle, it was difficult for the AFM probe to reach the bottom for such deep inverted-hollow-like BSi features. The AFM probe geometry restrained the detection of the bottom feature. Therefore, the depth of the structure at the artefact-free area appeared to be much shallower than the PFIB and AFM-HQ models.

2.3. Optical Reflectance Measurement

Optical characteristics were determined using a commercial PerkinElmer Lambda 1050 spectrophotometer to measure the wavelength-dependent total Reflection(%) (R_{Total}) and diffused Reflection(%) (R_{Diffuse}). Both the R_{Total} and R_{Diffuse} were measured using a 150 mm integrating sphere, with the BSi specimen placed on the reflectance port (see **Figure 4**). R_{Diffuse} was the measured scattered reflectance with specular exclusion port unplugged during the measurement. The incident beam was regulated into a 6 mm diameter circular beam by an adjustable iris, and a 6 mm reflectance aperture was mounted at the reflectance port before the beam hit the specimen. The measurement wavelength range was 250–1500 nm, with a step size of 5 nm. Due to the geometry of the accessory, the sample placed on the reflectance port was at an angle of 8° relative to the incident beam during the reflectance measurement.[35]

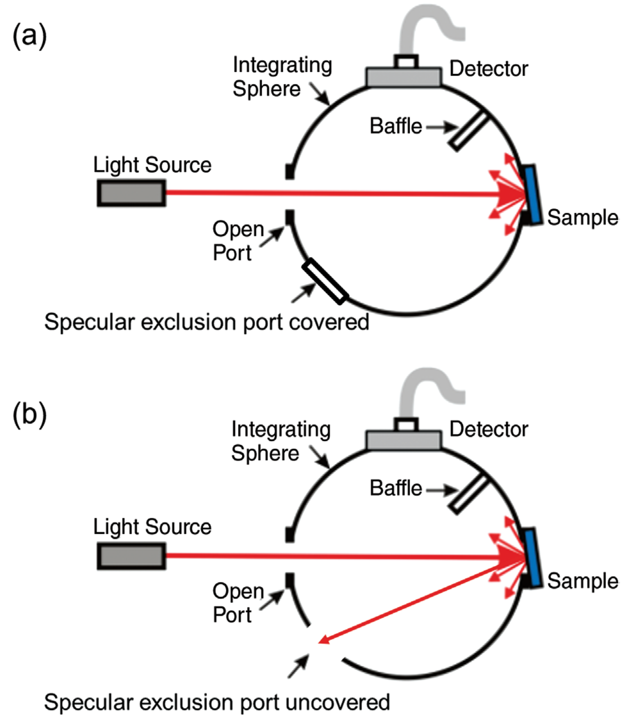

Figure 4. Measurement principle for a) R_{Total} and b) R_{Diffuse}. The dimension of the specular exclusion port is roughly 33 mm^2.

The R_{Total} and R_{Diffuse} were used for the calculation of specular reflectance (R_{Specular}) as defined in Equation (1)

$$R_{\text{Specular}} = R_{\text{Total}} - R_{\text{Diffuse}} \tag{1}$$

In addition, a double-side polished monocrystalline silicon wafer, with a thickness of 500 µm, was used as a reference reflectance standard. The measured reflectance was used to validate the simulation input: refractive index, n, and extinction coefficient, k.

2.4. Optical Simulation

Modeling of the Reflection(%) was performed using the Ansys Lumerical FDTD simulation package.[36] The obtained 3D AFM and PFIB surface models were used as geometric inputs to define the unit cell of the silicon–air interface, and the optical constants of silicon were defined using values from the

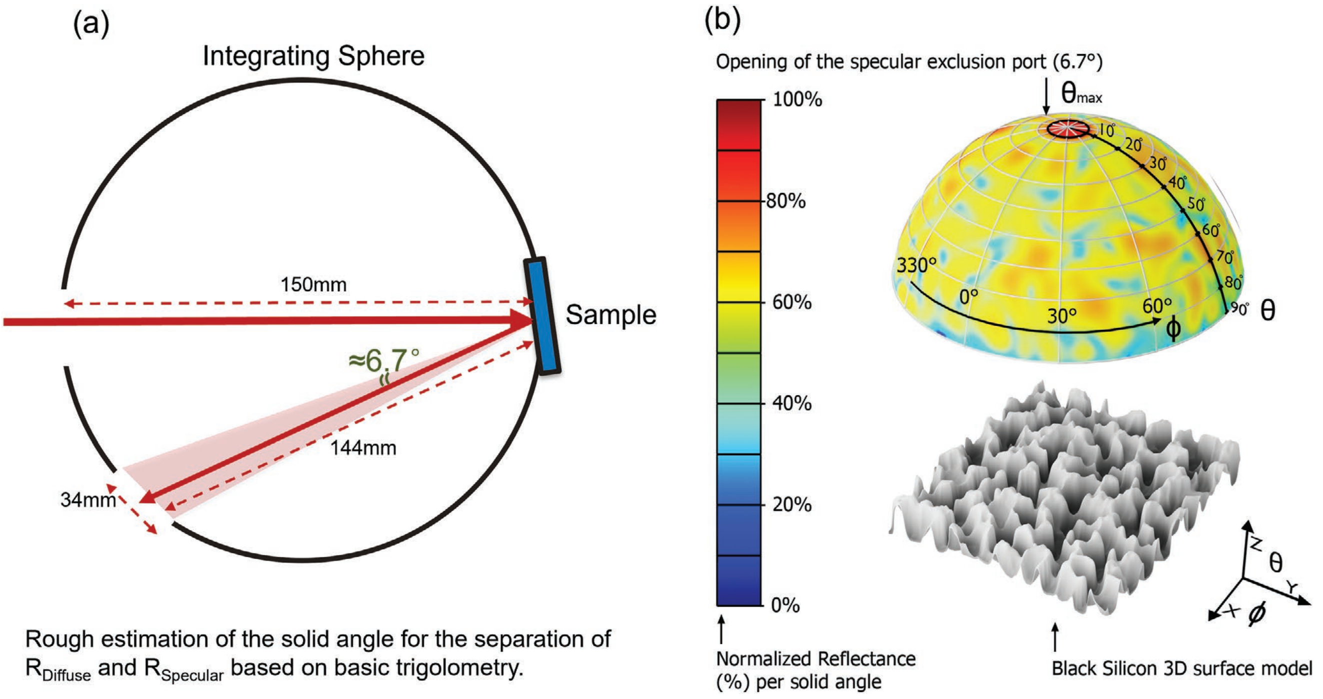

Figure 5. a) Estimated solid angle for the separation of R_{Diffuse} and R_{Specular} for FDTD simulation. The orientation and position of the BSi 3D model at the distance of $f = 144$ mm are clearly indicated. And b) illustration of a hemispherical far field reflectance modeling of the BSi surface structure.

literature.[37] Periodic boundary conditions were employed along the boundaries that intersect the surface, and perfectly matched layer (PML) boundary conditions in the out-of-plane direction–diffraction from the unit cell periodicity were excluded because the wavelength was much smaller than the lateral unit cell size (5 µm by 5 µm). Diffraction from the unit cell periodicity was found to be negligible when the lateral unit cell size (5 µm by 5 µm) was much larger than the wavelength—this was not the case when a unit cell length of 1–3 µm was used, or if the surface texture was not (semi-)random. The input source was a broadband plane-wave (wavelengths spanning 200–1000 nm); separate simulations were performed for s- and p-polarizations and then averaged for comparison to the unpolarized experimental data. The plane-wave was inserted at normal incidence instead of the experimental tilt of 8° because the resulting simulated reflection was almost identical, and modeling at normal incidence allowed for more robust simulation of all wavelengths in a single run, reducing the computational requirements.

A power monitor was positioned above the Si surface to collect the reflected light—this monitor in the near-field recorded the time-averaged electric field intensity, from which the simulated Reflection(%) was determined. To differentiate between the specular and diffuse parts of Reflection(%), Lumerical's built-in far field projection algorithm was used to obtain the calculated hemispherical reflection at a distance of 1 m (**Figure 5**). Analogous to the measurement, the intensity in the center of the hemisphere within 6.7° from the normal was calculated to obtain the specular/diffuse Reflection(%). The simulations were found to converge with a uniform mesh size of 5 nm in all directions, a distance of at least half the largest wavelength between the surface and the PML boundaries, and conformal mesh refinement.

3. Results and Discussion

3.1. Surface Statistics of RIE1 and RIE2 Extracted from Reconstructed 3D Models

A direct comparison between the sample's SEM and their 3D models reconstructed by either PFIB or AFM is shown in **Figure 6**; these images are all shown in plan-view. A qualitative comparison of these images can offer high-level insight into the accuracy of the models. The first impression from visual observation is that the PFIB models for both the BSi-RIE1 sample and the BSi-RIE2 sample retain the surface features revealed by SEM (groove-like for BSi-RIE1 and inverted-hollow-like for BSi-RIE2). In other words, the PFIB 3D models for both RIE1-BSi and RIE2-BSi show comparably better similarity than both AFM-HQ and AFM-LQ models. In contrast, both AFM reconstructed models are not similar to their corresponding SEM images. In particular, the deep inverted-hollow-like BSi-RIE2 sample was considered too aggressive for the AFM probe geometry, and the resulting AFM models are severely tilted due to the contacting angle of the AFM probe. Interestingly, both AFM scans (AFM-HQ and AFM-LQ) for RIE2-BSi were obtained with identical probe and characterization settings used for the AFM scanning. Nevertheless, they still show significant statistical differences because the RIE2 structure challenges the probe to operate under optimal conditions.

Under certain circumstances, the gray-scale SEM image of the specimen taken at various angles can provide an alternative for extracting the specimen's height distribution.[38] These conditions are: 1) when the BSi sample's feature is not too deep. In that case, most of the secondary electrons (SEs) generated from

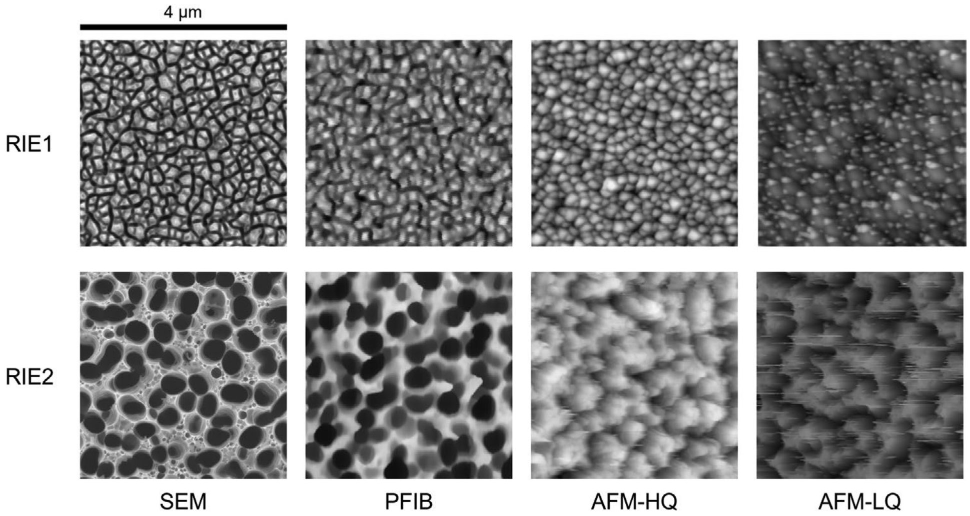

Figure 6. Plan view of the samples RIE1 and RIE2 obtained by SEM and from the 3D models reconstructed from the PFIB, AFM-HQ, and AFM-LQ measurements.

the specimen's surface, especially those from the bottom of the feature, will not be re-absorbed by the specimen. Therefore, the gray-scale SEM image can be calibrated well according to its SE pixel intensity (brightness); 2) a proper calibration is carried out in advance and an accurate monotonic correlation has been established between the pixel intensity and the local depth. However, both preconditions require additional effort to obtain reliable data, which in some cases are impossible. SEM image is made up of the pixel-wise intensity received by the SE detector. For samples like RIE2, the SE generated from the bottom will all be absorbed by the specimen's sidewalls, leaving the local pixel intensity to be zero. Therefore, once the "hollow-like" feature's depth is beyond a certain value, the "hollow-like" features are too deep to be distinguishable by SEM. As a comparison, PFIB data are made up of a stack of SEM images taken directly from the cross-sectional view of the specimen during each slice-and-view process. In other words, it has been self-validated by SEM. Therefore, we use the PFIB 3D model as a reference when comparing the surface statistical data.

The height distribution of RIE1 3D models and RIE2 3D models are displayed in **Figure 7**, where the *X*-axis represents the height values of each surface datapoint. The *Y*-axis represents the normalization of the density of the corresponding height value. The RIE1-PFIB and RIE1-AFM-HQ show similar height distributions (normal distribution), while the RIE1-AFM-LQ deviates quite significantly. For the RIE2-AFM-HQ and RIE2-AFM-LQ, the heights profiles are of comparable shape. However, the peak location of the RIE2-AFM-HQ profile was ≈0.5 µm deeper than the RIE2-AFM-LQ profile. This might be because the AFM probe could reach a deeper level of the structure while probing the surface after careful optimization. In comparison, the PFIB profile shows double peaks, one at ≈0.4 µm depth and one at ≈1.7 µm depth. This profile matches what has been observed in the SEM: the deep inverted-hollow-like textures of RIE2 had two dominant plateaus features.

Some critical surface statistical parameters extracted from the 3D surface models are listed in **Table 1**. Using the PFIB 3D model as a reference, the percentage value in the bracket means how much the AFM 3D model extracted parameter deviated from the PFIB model (if applicable).

The first parameter is the mean square roughness (RMS), which describes the irregularity of height data values. The

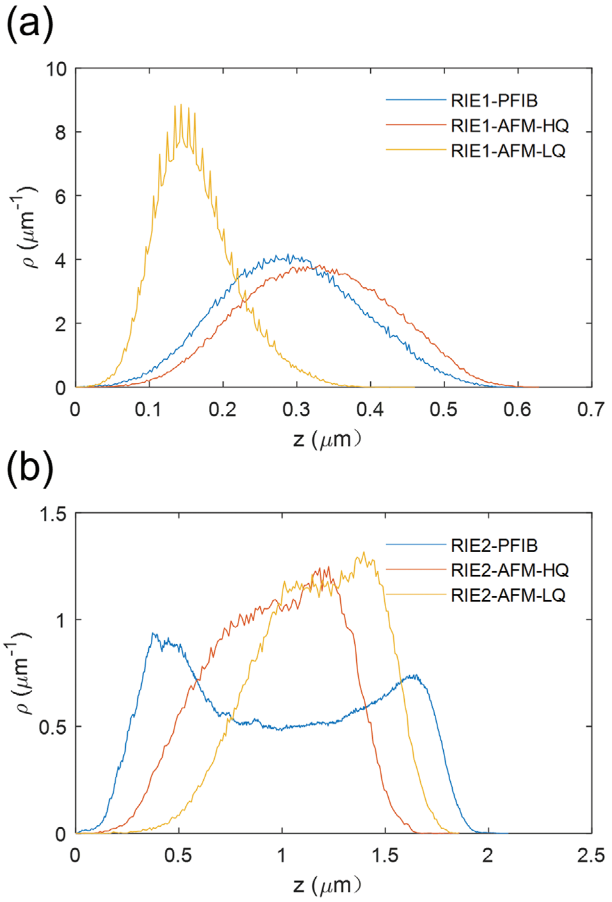

Figure 7. Height distribution of a) RIE1 and b) RIE2 extracted from PFIB 3D model and AFM 3D model.

Table 1. Critical surface statistical parameters for BSi-RIE1 and BSi-RIE2, extracted by 3D models of PFIB, AFM-HQ, and AFM-LQ.

	BSi-RIE1			BSi-RIE2		
	PFIB	AFM-HQ	AFM-LQ	PFIB	AFM-HQ	AFM-LQ
RMS	93.6	96.8 (+3.4%)	54.8 (−41.5%)	487.2	279.5 (−42.6%)	296.9 (−39.1%)
Ssk	0.09	0.01	0.62	0.09	−0.30	−0.21
EAF	3.07	2.91 (−5.3%)	1.63 (−46.7%)	5.65	4.20 (−25.7%)	4.84 (−14.2%)
SSA	10.47	8.87 (−15.3%)	9.98 (−4.7%)	5.76	3.58 (−38.0%)	5.02 (−12.8%)

reported RMS for RIE1-AFM-HQ and RIE1-PFIB was of comparable value, while the RMS of RIE2-AFM-HQ is only half that of RIE2-PFIB. This is because, unlike the BSi-RIE1, the BSi-RIE2 is too deep for the AFM probe-sample interaction. Therefore, the resulting RIE2-AFM-HQ rendered 3D model is not as rough as the RIE2-PFIB model, with an RMS value of less than half of the RIE2-PFIB.

Another parameter, skewness (Ssk), describes the degree of bias of the roughness features(asperity). A symmetrical structure (relative to the mean plane) will have zero Ssk value. If the height distribution is skewed above the mean plane, Ssk will report a negative value and vice versa. As a comparison, RIE1-AFM-HQ and RIE1-PFIB are similar and have height distributions that are slightly skewed above the mean plane. RIE2-AFM-HQ and RIE2-PFIB, however, are of opposite values, indicating their height distributions are inversely skewed.

The last two parameters, enhanced area factor (EAF) and specific surface area (SSA), describe the surface enlargement. The EAF describes the ratio of the total surface area to the projected planar area, which is most widely used in the literature. The SSA, defined as the ratio of the surface area to the volume of the underlying silicon nanofeature, was recently introduced to BSi in our previous work.[30] It is directly related to surface reactivity and found to be a better indicator of the surface chemical reaction rate.[30] Both BSi-RIE1 and BSi-RIE2 reported the highest EAF and SSA values from the PFIB 3D model. The SSA for the RIE1-AFM-HQ is reported to be 15.3% less than the RIE1-PFIB, while the SSA for the RIE2-AFM-HQ is 38.0% less than the RIE2-PFIB. As the SSA describes the ratio between the surface atoms to the internal atoms within the defined volume, the AFM-HQ model will report underestimated surface reactivity if used as simulation input.

3.2. Simulated Hemispherical Reflectance

The FDTD simulated hemispherical reflectance results for both RIE1-PFIB and RIE2-PFIB are depicted in **Figure 8**. As demonstrated in previous research, the reflectance spectrum for crystalline silicon exhibits two distinct peaks, E1 (≈365 nm) and E2 (≈275 nm),[39–41] which are correlated with silicon material quality, such as the absorption coefficient,[39,42] refractive index,[39,42] and dielectric function.[42,43] In particular, the E2 peak is highly correlated to surface roughness. Therefore, our group's previous work has extended the use of E1 and E2 peaks into a 2D mapping for surface texturing.[44] The FDTD simulation results show that the reflection for both RIE1 and RIE2 are well scattered at E1 and E2 peaks, which explains the root cause of the excellent optical behavior of BSi.

3.3. Comparison of the Measured Reflectance Data

The measured optical reflectance [Reflection(%)] characteristics, including R_{Total}, R_{Diffuse}, and R_{Specular}, for both RIE1 and RIE2 are shown in **Figure 9** as the bold blue line. The comparison of Reflection(%) results between RIE1 and RIE2 indicates that differences in the surface nanostructure morphology impact the reflectance characteristics. The BSi-RIE2 sample was superior in low reflectance and showed much-suppressed surface reflectance compared to the BSi-RIE1 sample.

To further evaluate the quality of the AFM 3D model and the PFIB 3D model, we use the convergence of the FDTD simulated reflection to the measured Reflection(%) for quantitative evaluation.

The comparison between the measured Reflection(%) and FDTD simulated reflectance based on the 3D surface model obtained by PFIB and AFM approaches is also shown in Figure 9.

For RIE1, both PFIB-Reflection(%) and AFM-HQ-Reflection(%) are shown to be in good agreement with the measured Reflection(%). Surprisingly, for RIE2, the AFM-HQ-Reflection(%) still agrees well with the measured Reflection(%), although differences in surface morphology can be observed both visually and from the statistical results reported in Table 1. This suggests that the extra deep inverted-hollow features, which are not detectable by the AFM probe, do not significantly contribute to a reduction in reflection in this case. Therefore, the resulting FDTD simulated Reflection(%) from the AFM-HQ model is about the same level as the PFIB model. The PFIB-FDTD of RIE1 is closer to the measured Reflection(%) at the UV range, while the AFM-HQ-FDTD is closer to the measured Reflection(%) at the VIS and NIR (below bandgap) range.

The Reflection(%) measurement settings had an incident beam angle of 8° relative to the sample's zenith. However, the FDTD simulation was carried out with a normal incident beam, as plane-wave simulation with a broad wavelength span and angled-incidence would drastically increase the computational cost. Such differences in the simulation settings may be the reason for the small mismatch between the PFIB/AFM-HQ simulated Reflection(%) and measured Reflection(%). However, other factors may also contribute to the simulation/measurement discrepancy, such as the difference between the simulation scale (on the order of square micrometers) to the measurement scale (on the order of square millimeters).

In contrast, the AFM-LQ-FDTD for both BSi-RIE1 and BSi-RIE2 drastically deviates from the measured Reflection(%) data. The surface morphology difference and statistical results also provide strong evidence that the 3D model does not accurately represent the true surface structure and characteristics of the actual BSi sample. As AFM probing is highly sensitive to

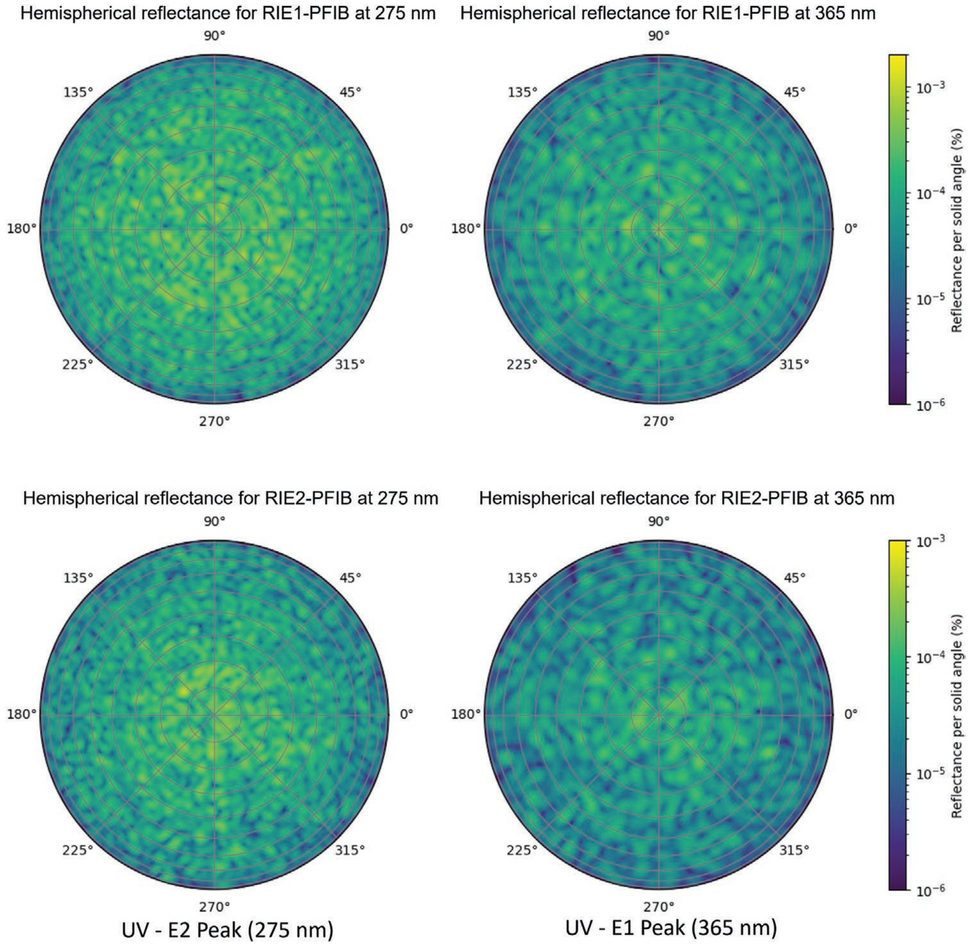

Figure 8. Simulated hemispherical reflectance of RIE1-PFIB (top row) and RIE2-PFIB (bottom row) at the E1 and E2 peaks.

experimental settings, there is a high chance that an erroneous surface model will be obtained. However, the surface rendered by PFIB tomography was based on the information extracted from the specimen's SEM images obtained during the slice-and-view, which could be directly checked against the bare specimen's cross-sectional SEM taken before the PFIB sampling. The detailed PFIB sampling method was described in detail in our previous work[14] and is less likely to obtain bias or artefacts when reconstructing the surface 3D model.

In addition to the reflectance line plots, the statistical convergence between the FDTD simulated reflectance and the measured reflectance was also calculated. The root-mean-square-error (RMSE) (as defined in Equation (2)) was used for convergence evaluation, indicating how much in proportional the squared errors are between the FDTD simulated Reflection(%) and the measured Reflection(%). The results are shown in **Table 2**

$$\mathrm{RMSE}(\%) = \sqrt{\frac{\int (R_{\mathrm{FDTD}} - R_{\mathrm{Measured}})^2 \, \mathrm{d}\lambda}{\int (R_{\mathrm{Measured}})^2 \, \mathrm{d}\lambda}} \times 100\% \tag{2}$$

From Table 2, we can see that the FDTD simulated Reflection(%) for both the PFIB 3D model and the AFM-HQ 3D model were close to the measured Reflection(%) data for sample RIE1-BSi. The RMSE of RIE1-PFIB and RIE1-AFM-HQ was similar. For total reflectance, both PFIB and AFM-HQ were around 0.2, while the RMSE of RIE1-AFM-LQ was reported to be 2.6, which is around ten times higher than the other two. Table 2 also shows that the FDTD simulated data for the PFIB 3D model remains at the same level for Sample RIE2. At the same time, the AFM-LQ deviated drastically with an RMSE of 7.31 over the whole wavelength range, around 20 times greater than that of the RIE2-PFIB data.

Our group reported previously that the UV reflectance behavior is particularly sensitive to surface nanoetching.[44] As such, an UV reflectance map can be used to quickly monitor texturing variation. Therefore, Table 2 also shows the deviation of FDTD simulated Reflection(%) to the measured Reflection(%) in the UV (250–400 nm) only range. In this range, the RMSE between the AFM-LQ Reflection(%) to the measured Reflection(%) for BSI-RIE1 is one order of magnitude higher than the PFIB Reflection(%) and AFM-HQ Reflection(%). In particular, the RMSE of AFM-LQ simulated R_{Diffuse} for BSi-RIE2 was nearly 200 times higher than the PFIB simulated R_{Diffuse}. This further supports the hypothesis that the BSi-RIE2 AFM-LQ 3D model poorly represents the true surface structure and corresponding optical performance.

Comparing the 3D models rendered from PFIB tomography and AFM, the PFIB 3D models qualitatively represent the

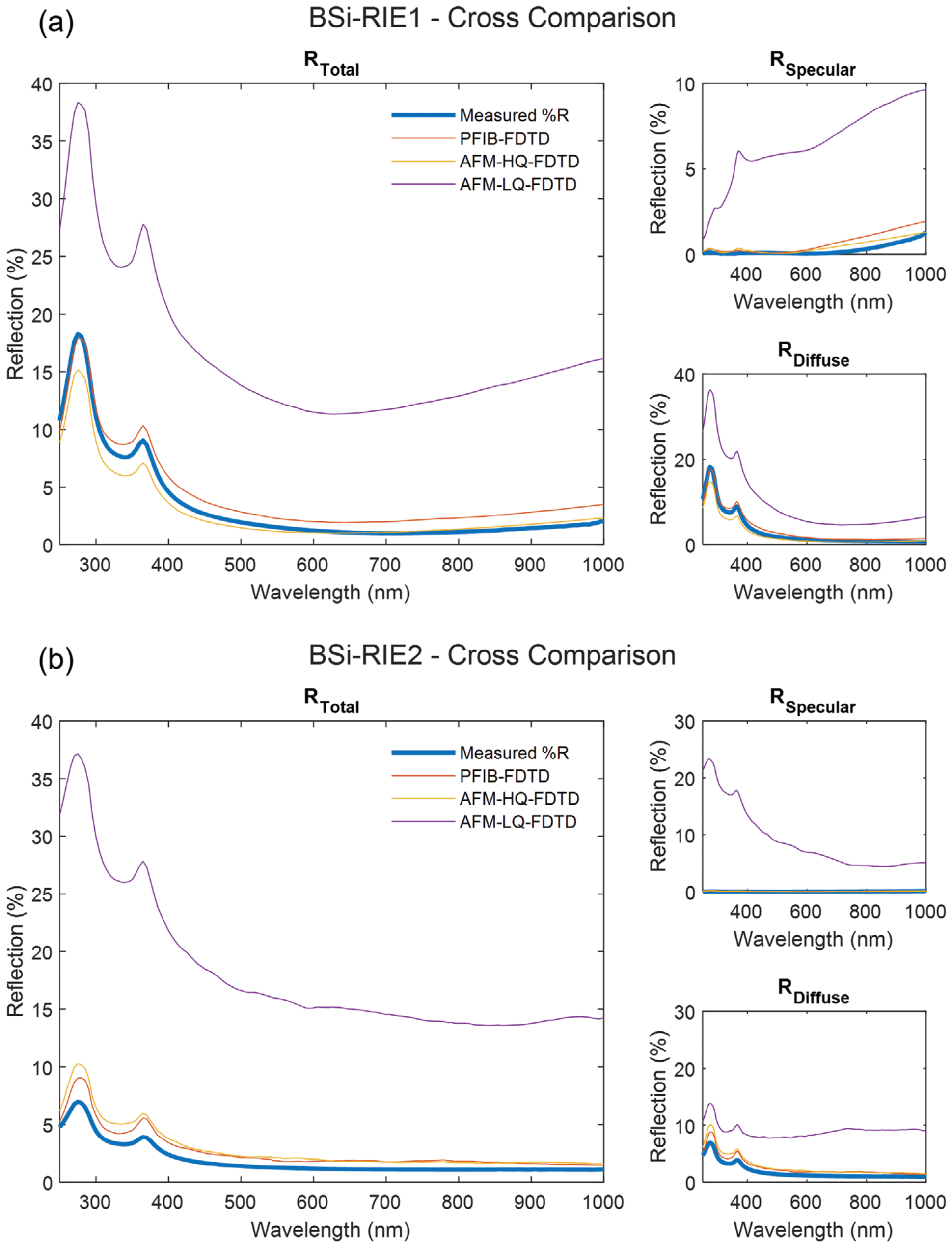

Figure 9. Cross-comparison of the R_{Total}, the R_{Diffuse}, and the R_{Specular} for a) BSi-RIE1 and b) BSi-RIE2.

Table 2. Statistic comparison of the FDTD simulated reflectance and the measured reflectance(%) for sample RIE1 and RIE2, evaluated by RMSE.

		RIE1 – RMSE			RIE2 – RMSE		
		PFIB	AFM-LQ	AFM-HQ	PFIB	AFM-LQ	AFM-HQ
R_{Total}	Full λ range (250–1000 nm)	21.5%	260.4%	18.8%	38.3%	731.0%	51.6%
	UV (250–400 nm)	9.0%	163.2%	18.6%	30.8%	557.7%	47.9%
R_{Specular}	Full λ range (250–1000 nm)	127.7%	1633.4%	63.6%	110.9%	21972.3%	87.6%
	UV (250–400 nm)	241.4%	6176.7%	289.1%	460.8%	83965.5%	3.9%
R_{Diffuse}	Full λ range (250–1000 nm)	14.4%	134.1%	20.5%	36.6%	318.3%	50.5%
	UV (250–400 nm)	8.3%	77.0%	20.2%	28.7%	136.7%	46.2%

sample's real morphology more accurately. By summarizing the statistical results presented in Table 1, we found that the PFIB 3D model for both RIE samples reports a much higher surface roughness and area-to-volume ratio, which could be linked to a much greater chemical reaction rate. Table 2 demonstrates that the PFIB 3D model shows the closest match between the measured Reflection(%) and FDTD simulated Reflection(%). Consequently, it is clear that our work provides strong evidence that PFIB tomography is more accurate compared to AFM for determining the surface topography, especially for highly roughened BSi surfaces. PFIB can be used for extreme BSi surfaces with features such as vertical sidewalls or overhanging structures, which cannot be assessed by AFM probing. Consequently, PFIB enables a more accurate prediction of the performance of devices that employ BSi in areas such as PV,[45,46] photo-current sensors,[47–51] photoelectrochemical devices,[52–57] biosensors,[58,59] etc.

4. Conclusion

In this work, we compared various surface statistical parameters generated from PFIB 3D and AFM 3D models of BSi, which should correlate to the BSi surface optical and electrochemical performances. For a shallower textured surface with small groove-like features (RIE1), PFIB 3D model and AFM-HQ 3D model resulted in similar values for most surface profile parameters, such as RMS and Ssk, indicating that both surface models are in good agreement. However, two models generated different SSA values, a vital input parameter for predicting the surface chemical reaction rates, PFIB model reported a higher SSA value. For a more challenging deeper textured surface with inverted-hollow-like features (RIE2), the surface profile parameters from PFIB and AFM-HQ models deviate quite far, indicating that the reconstructed 3D surface generated from PFIB and AFM could have different surface morphology. Similarly, SSA value from PFIB is much higher than the AFM-HQ model.

Even though surface topography statistics from two models were proven to be dissimilar to each other, both PFIB and AFM-HQ show good convergence to measured Reflection(%) when used as input parameters for FDTD front surface reflectance simulation. Both can be used to accurately predict the optical performance of BSi. By contrast, the AFM-LQ 3D modeled parameters deviate from the measured reflectance severely, which is tenfold greater than AFM-HQ to PFIB. In particular, the RMSE for RIE2-AFM-LQ in the UV range is as high as 83965.5%, indicating the data are significantly deviating from the measured Reflection(%).

In summary, AFM for BSi surface topographical characterization is highly dependent on the AFM probe and parameters settings, with significant potential for erroneous results. Our work provides strong evidence that PFIB tomography is a better substitute to the AFM for surface topographical characterization, especially in probing highly roughened BSi surfaces. While PFIB is a destructive technique and may take longer than the conventional AFM approach, it has the benefit of consistent and easily validated results by SEM. It can be used for extreme BSi surfaces with features such as vertical sidewalls or overhanging structures, which are not compatible with AFM probing. In the future, PFIB tomography, as a substitute for AFM surface probing technology, provides a pathway to accurately obtain the 3D model for BSi surface or other nanotextured structures. Such an accurate 3D model can be used as simulation input for first-principle simulation. The validated simulation results can further aid in developing and validating fast approximation methods for optical device simulation, such as effective medium and geometric optics, assisting in reducing the computational cost for BSi device simulation.

Acknowledgements

This work was supported by funding from the Australian government via the ARENA 2017/RND009 project. The authors acknowledge the facilities, and the scientific and technical assistance of the Australian Microscopy & Microanalysis Research Facility at the Electron Microscope Unit, The University of New South Wales. The responsibility for the views, information, or advice expressed herein is not accepted by the Australian government. This work was also supported by the Dutch Research Council (NWO) and was partly carried out on the Dutch national e-infrastructure with the support of SURF Cooperative. The BSi-RIE sample fabrication was supported by the Velux Foundation project no. 13891 in Denmark. The authors thank Rasmus S. Davidsen from the Technical University of Denmark for helping with the BSi sample fabrication. The authors thank Charlie Kong from the Electron Microscope Unit of UNSW for helping with the PFIB tomography work. The authors thank Yin Yao from the Electron Microscope Unit of UNSW for helping with the AFM characterization work.

Open access publishing facilitated by University of New South Wales, as part of the Wiley–University of New South Wales agreement via the Council of Australian University Librarians.

Conflict of Interest

The authors declare no conflict of interest.

Author Contributions

In this manuscript, Y.Z. conducted the AFM and PFIB characterization and wrote the original draft. T.V. performed the FDTD simulations. Both Y.Z. and T.V. contributed to the data analysis, results discussion, reviewed and edited the manuscript. D.P., B.H., and A.P. supervised this work, reviewed and edited the manuscript. S.W., G.S., and M.A. contributed to different stages of conceptualization, methodology, reviewing, and editing.

Data Availability Statement

The data that support the findings of this study are available from the corresponding author upon reasonable request.

Keywords

black silicon, FDTD, full wave optical simulation, PFIB tomography

Received: January 13, 2022
Revised: March 26, 2022

---

[1] X. Liu, P. R. Coxon, M. Peters, B. Hoex, J. M. Cole, D. J. Fray, *Energy Environ. Sci.* **2014**, *7*, 3223.
[2] J. Lv, T. Zhang, P. Zhang, Y. Zhao, S. Li, *Nanoscale Res. Lett.* **2018**, *13*, 110.
[3] Y. Xia, B. Liu, J. Liu, Z. Shen, C. Li, *Sol. Energy* **2011**, *85*, 1574.

[4] R. R. Bilyalov, R. Lüdemann, W. Wettling, L. Stalmans, J. Poortmans, J. Nijs, L. Schirone, G. Sotgiu, S. Strehlke, C. Lévy-Clément, *Sol. Energy Mater. Sol. Cells* **2000**, *60*, 391.

[5] M. Ben Rabha, W. Dimassi, M. Bouaïcha, H. Ezzaouia, B. Bessais, *Sol. Energy* **2009**, *83*, 721.

[6] T. Pasanen, V. Vähänissi, N. Theut, H. Savin, *Energy Procedia* **2017**, *124*, 307.

[7] J. Wu, H. Wu, X. Chen, Z. Yao, D. Zhang, S. Su, M. Zhang, F. Jiang, G. Xing, in *2019 IEEE 46th Photovolt. Spec. Conf.* (Ed: S. Kurtz), IEEE, Chicago, IL, USA **2019**, pp. 1466–1470.

[8] M. U. Khan, G. Scardera, S. Zou, D. Zhang, M. Abbott, *IEEE J. Photovoltaics* **2021**, *11*, 627.

[9] F. Shimura, *Semiconductor Silicon Crystal Technology*, Elsevier Science, New York **2012**.

[10] Synopsys, Sentaurus Device – An advanced multidimensional (1D/2D/3D) device simulator, https://www.synopsys.com/silicon/tcad/device-simulation/sentaurus-device.html (accessed: November 2021).

[11] PV Lighthouse, SunSolve^{TM} - v 4.0.11, **2019**, https://www.pvlighthouse.com.au/sunsolve.

[12] K. Füchsel, M. Kroll, M. Otto, M. Steglich, A. Bingel, T. Käsebier, R. B. Wehrspohn, E. B. Kley, T. Pertsch, A. Tünnermann, M. Algasinger, H. Branz, B. Gesemann, T. Gimpel, K. Füchsel, T. Käsebier, S. Kontermann, S. Koynov, X. Li, V. Naumann, J. Oh, A. N. Sprafke, J. Ziegler, M. Zilk, R. B. Wehrspohn, *Photon Manage. Sol. Cells* **2015**, *3*, 117.

[13] B. Bhushan, in *Modern Tribology Handbook. Vol. 1, Principles of Tribology*, CRC Press, Boca Raton, FL **2000**, pp. 79–150.

[14] Y. Zhang, C. Kong, R. S. Davidsen, G. Scardera, L. Duan, K. T. Khoo, D. N. R. Payne, B. Hoex, M. Abbott, *Ultramicroscopy* **2020**, *218*, 113084.

[15] F. J. Giessibl, *Rev. Mod. Phys.* **2003**, *75*, 949.

[16] N. Jalili, K. Laxminarayana, *Mechatronics* **2004**, *14*, 907.

[17] D. Sarid, *J. Vac. Sci. Technol., B: Microelectron. Nanometer Struct.–Process., Meas., Phenom.* **1991**, *9*, 431.

[18] E. Ukraintsev, A. Kromka, H. Kozak, B. Rezek, Z. Reme, B. Rezek, *Atomic Force Microscopy Investigations into Biology – From Cell to Protein*, IntechOpen, London, UK **2012**.

[19] J. I. Paredes, A. Martinez-Alonso, J. M. D. Tascon, *J. Microsc.* **2000**, *200*, 109

[20] U. D. Schwarz, H. Haefke, P. Reimann, H.-J. Güntherodt, H. Guntherodt, *J. Microsc.* **1994**, *173*, 183.

[21] T. H. Fung, T. Veeken, D. Payne, B. Veettil, A. Polman, M. Abbott, *Opt. Express* **2019**, *27*, 38645.

[22] S. Chattopadhyay, Y. F. Huang, Y. J. Jen, A. Ganguly, K. H. Chen, L. C. Chen, *Mater. Sci. Eng., R* **2010**, *69*, 1.

[23] T. H. Fung, M. U. Khan, Y. Zhang, N. J. Western, D. N. R. R. Payne, K. R. McIntosh, M. D. Abbott, K. R. McIntosh, M. D. Abbott, *IEEE J. Photovoltaics* **2019**, *9*, 591.

[24] K. Tang, R. A. Dimenna, R. O. Buckius, *Int. J. Heat Mass Transfer* **1996**, *40*, 49.

[25] Y. Ge, F. Zhao, L. Wang, X. Wang, *Surf. Coat. Technol.* **2020**, *402*, 126493.

[26] M. Steglich, T. Käsebier, M. Zilk, T. Pertsch, E. B. Kley, A. Tünnermann, *J. Appl. Phys.* **2014**, *116*, 173503.

[27] S. Ma, S. Liu, Q. Xu, J. Xu, R. Lu, Y. Liu, Z. Zhong, *AIP Adv.* **2018**, *8*, 035010.

[28] M. Kroll, T. Käsebier, M. Otto, R. Salzer, R. B. Wehrspohn, E.-B. Kley, A. Tünnermann, T. Pertsch, *Proc. SPIE* **2010**, *7725*, 772505.

[29] D. Payne, T. H. Fung, M. U. Khan, J. Cruz-Campa, K. McIntosh, M. Abbott, *AIP Conf. Proc.* **2018**, *1999*, 050007.

[30] G. Scardera, S. Wang, Y. Zhang, M. U. Khan, S. Zou, D. Zhang, R. S. Davidsen, O. Hansen, L. Mai, D. N. R. R. Payne, B. Hoex, M. D. Abbott, *IEEE J. Photovoltaics* **2021**, *11*, 298.

[31] D. Payne, M. Abbott, A. C. Lopez, Y. Zeng, T. H. Fung, J. Cruz-campa, R. Davidson, M. Plakhotnyuk, D. Bagnall, in *33rd Eur. Photovolt. Sol. Energy Conf. Exhib.* (Eds: A. Smets, P. Helm, N. Taylor), WIP – Renewable Energies, Amsterdam, The Netherlands **2017**, pp. 897–901.

[32] A. Fell, K. C. Fong, K. R. McIntosh, E. Franklin, A. W. Blakers, *IEEE J. Photovoltaics* **2014**, *4*, 1040.

[33] Y. Zhang, C. Kong, M. U. Khan, T. H. Fung, R. S. Davidsen, O. Hansen, G. Scardera, M. D. Abbott, B. Hoex, D. N. R. Payne, C. Kong, M. U. Khan, T. H. Fung, R. S. Davidsen, O. Hansen, G. Scardera, M. D. Abbott, B. Hoex, in *2019 IEEE 46th Photovolt. Spec. Conf.* (Ed: S. Kurtz), IEEE, Chicago, IL, USA **2019**, pp. 0825–0828.

[34] Y. Zhang, C. Kong, G. Scardera, M. Abbott, D. N. R. Payne, B. Hoex, *Ultramicroscopy* **2021**, *233*, 113458.

[35] PerkinElmer and Labsphere®, LAMBDA 650/750/850/950/1050 Accessories for LAMBDA Series, https://www.perkinelmer.com/CMSResources/Images/44-135972BRO_009201B_0LambdaAccessories.pdf (accessed: August 2020).

[36] Lumerical, FDTD Solution, https://www.lumerical.com/products/fdtd/ (accessed: September 2021).

[37] E. D. Palik, *Handbook of Optical Constants of Solids*, Elsevier, New York **1985**.

[38] E. Ponz, J. L. Ladaga, R. D. Bonetto, *Microsc. Microanal.* **2006**, *12*, 170.

[39] H. R. Philipp, E. A. Taft, *Phys. Rev.* **1960**, *120*, 37.

[40] M. A. Green, *Sol. Energy Mater. Sol. Cells* **2008**, *92*, 1305.

[41] M. Welkowsky, R. Braunstein, *Phys. Rev. B* **1972**, *5*, 497.

[42] G. E. Jellison, *Opt. Mater.* **1992**, *1*, 151.

[43] W. Theiß, M. Miu, I. Kleps, T. Ignat, M. Simion, A. Bragaru, W. Theiß, *Surf. Sci. Rep.* **1997**, *29*, 91.

[44] G. Scardera, D. N. R. Payne, M. U. Khan, Y. Zhang, A. Soeriyadi, S. Zou, D. Zhang, R. S. Davidsen, O. Hansen, B. Hoex, M. D. Abbott, *IEEE J. Photovoltaics* **2021**, *11*, 1291.

[45] H. C. Yuan, V. E. Yost, M. R. Page, P. Stradins, D. L. Meier, H. M. Branz, *Appl. Phys. Lett.* **2009**, *95*, 123501.

[46] H. M. Branz, V. E. Yost, S. Ward, K. M. Jones, B. To, P. Stradins, *Appl. Phys. Lett.* **2009**, *94*, 231121.

[47] F. Patolsky, G. Zheng, C. M. Lieber, *Anal. Chem.* **2006**, *78*, 4260.

[48] F. Patolsky, B. P. Timko, G. Zheng, C. M. Lieber, N. Field, E. Sensors, F. Patolsky, P. Brian, B. P. Timko, G. Zheng, C. M. Lieber, N. Field, E. Sensors, F. Patolsky, P. Brian, *MRS Bull.* **2007**, *32*, 142.

[49] M. J. Schmand, D. Henseler, R. Grazioso, N. Zhang, M. S. Andreaco, *US 2010/0074396 A1*, **2010**.

[50] M. U. Pralle, J. E. Carey, H. Homayoon, S. Alie, J. Sickler, C. Palsule, J. Mckee, X. Li, J. Jiang, D. Miller, C. Palsule, J. Mckee, *Proc. SPIE* **2010**, *7660*, 76600N.

[51] G. Seniutinas, G. Gervinskas, R. Verma, B. D. Gupta, F. Lapierre, P. R. Stoddart, F. Clark, S. L. Mcarthur, S. Juodkazis, *Opt. Express* **2015**, *23*, 6763.

[52] A. P. Goodey, S. M. Eichfeld, K. K. Lew, J. M. Redwing, T. E. Mallouk, U V Park, V. Pennsyl, *J. Am. Chem. Soc.* **2007**, *129*, 12344.

[53] J. R. Szczech, S. Jin, *Energy Environ. Sci.* **2011**, *4*, 56.

[54] J. Oh, T. G. Deutsch, H. C. Yuan, H. M. Branz, E. Environ, J. Oh, T. G. Deutsch, H. C. Yuan, H. M. Branz, E. Environ, J. Oh, T. G. Deutsch, H. C. Yuan, H. M. Branz, *Energy Environ. Sci.* **2011**, *4*, 1690.

[55] I. Oh, J. Kye, S. Hwang, *Nano Lett.* **2012**, *12*, 298.

[56] R. Carter, S. Chatterjee, E. Gordon, K. Share, W. R. Erwin, A. P. Cohn, R. Bardhan, C. L. Pint, *Nanoscale* **2015**, *7*, 16755.

[57] Y. Yu, Z. Zhang, X. Yin, A. Kvit, Q. Liao, Z. Kang, X. Yan, Y. Zhang, X. Wang, *Nat. Energy* **2017**, *2*, 17045.

[58] Y. L. Deng, Y. J. Juang, *Biosens. Bioelectron.* **2014**, *53*, 37.

[59] E. P. Ivanova, J. Hasan, H. K. Webb, G. Gervinskas, S. Juodkazis, V. K. Truong, A. H. F. F. Wu, R. N. Lamb, V. A. Baulin, G. S. Watson, J. A. Watson, D. E. Mainwaring, R. J. Crawford, *Nat. Commun.* **2013**, *4*, 2838.